Growth kinetics and structure of fibrin gels

F. Ferri* and M. Greco
Dipartimento di Scienze Chimiche, Fisiche e Matematiche, and INFM, Universita' dell'Insubria at Como, via Valleggio 11, 22100 Como, Italy

G. Arcovito, F. Andreasi Bassi, and M. De Spirito
Istituto di Fisica, Facolta' di Medicina e Chirurgia and INFM, Universita' Cattolica del Sacro Cuore, L.go F.Vito 1, 00168 Roma, Italy

E. Paganini
ENEL-Ricerca, via Andrea Pisano, 120-56122 Pisa, Italy

M. Rocco
UO Biologia Strutturale, Istituto Nazionale per la Ricerca sul Cancro (IST), c/o Centro Biotecnologie Avanzate (CBA), Largo R. Benzi 10, 16132 Genova, Italy

(Received 31 July 2000; published 14 February 2001)

The structure and kinetics of fibrin gels grown from fibrinogen solutions under quasiphysiological conditions, but in absence of Ca^{++}, were investigated by means of elastic light scattering. By combining classical light scattering and low-angle elastic light scattering, an overall wave-vector range of about three decades was spanned, from $q \sim 3\times10^{2}$ to $q \sim 3\times10^{5}\ \mathrm{cm}^{-1}$. The scattered intensity distribution of the gels was measured in absolute units and fitted to a single function, which was able to reproduce accurately the data over the entire wave-vector range. From the fitting, it was possible to estimate the average diameter d of the fibrin fibers, the average crossover length ξ of the gel, and establish the fractal nature of the gel structure, with a measure of its fractal dimension D_m. The measure of the intensity in absolute units also allowed the estimate of the density ρ of the fibrin fibers and provided an independent measure of their size. The kinetics of formation of the gel was described in terms of a simple growth model: the scaffold of the network is formed very early in the course of the gelation process, at a ''networking time,'' t_n, which is much smaller than the time required to form the final gel. At times $t > t_n$, the gel structure remains substantially unchanged and the successive growth consists only in a thickening of the gel fibers. Gels prepared under the same physical–chemical conditions, but at different fibrinogen concentrations, exhibited rather similar structures and kinetics, showing that the modalities of the gelation process are mainly governed by the solution conditions, and only secondarily by the fibrinogen concentration. For gels at fibrinogen concentration of $\sim$0.24 mg/ml, the gel parameters were $d \sim 130$ nm, $\xi \sim 27\ \mu$m, $D_m \sim 1.3$, and $\rho \sim 0.4\ \mathrm{g/cm}^3$. Our d and ρ values are in very good agreement with electron microscopy- and turbidity-derived literature data, respectively, while ξ seems to be related to the mesh size of the initial scaffold formed at t_n, rather than to the mesh size of the final aged gel.

DOI: 10.1103/PhysRevE.63.031401 PACS number(s): 82.70.−y, 87.15.Nn, 82.35.−x

I. INTRODUCTION

Fibrin gels are biological networks of fundamental importance in blood coagulation processes and in many other emorheological situations. They are grown from the polymerization of fibrinogen, a glycoprotein present in the plasma of vertebrates, after activation by the action of some specific enzyme, such as thrombin in the physiological case [1–3]. Fibrinogen is a centrosymmetric high molecular weight macromolecule ($MW = 340\,000$) rodlike in shape, $\sim$50 nm long, and $\sim$3–6 nm thick [see Fig. 1(a)]. Basically, the molecule consists of a central globular domain joined to two outer globular domains by two extended connectors, as shown early by electron microscopy [4] (see also [2], and references therein), and recently confirmed by crystallographic studies [5,6]. The central domain contains two pairs of the bonding sites *A* and *B*, which are masked by two pairs of short peptides called fibrinopeptides A and B (FPA and FPB), respectively. The polymerization sites *a* and *b* (complementary to the sites *A* and *B*), are at the extremities of the outer domains, where other sites, susceptible of enzymatic cross-linking, are also located (not involved in this work).

When fibrinogen interacts with thrombin, it becomes a reactive protein called monomeric fibrin. This activation occurs by cleavage of the two FPAs and FPBs from the central domain of the molecules, making the binding sites *A* and *B* exposed for noncovalent, knob-hole type interactions with the corresponding complementary sites *a* and *b* on another molecule [see Figs. 1(b) and 1(c)]. The *aA* interactions are responsible for linear aggregation, while the *bB* enhance the lateral growth of the fibrin fiber. The cleavage mechanism of thrombin, however, is slightly peculiar, consisting first in the cleavage of the FPAs, and only successively of the FPBs. Thus at the beginning, the monomers grow linearly, forming two-stranded, half-staggered chains known as protofibrils [see Figs. 1(c) and 1(d)]. Later on, when the sites *B* start to be activated and/or the protofibrils have reached some criti-

*Corresponding author. Electronic address: ferri@fis.unico.it

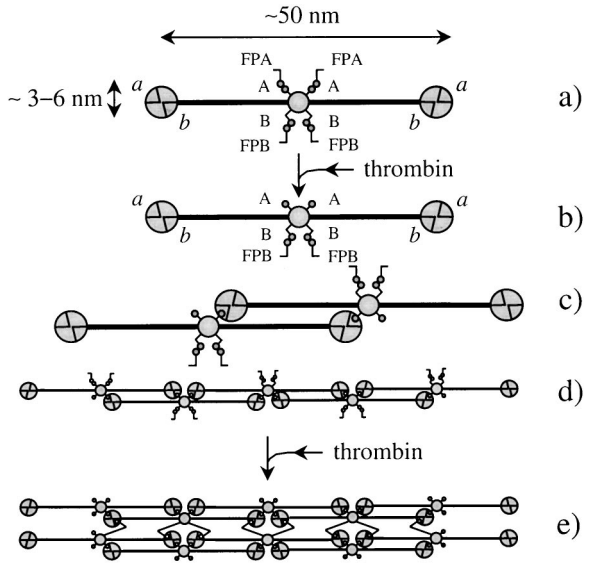

FIG. 1. Schematic models of fibrinogen and its basic polymerization mechanism. (a) In the unactivated molecule, the two pairs of polymerization sites *A* and *B* in the central domain are masked by the fibrinopeptides FPA and FPB. (b) Upon activation by the enzyme thrombin, the two FPAs are removed. (c) Dimers are formed via *aA* noncovalent interactions of sites *A* with complementary sites *a*, always available in the outer domains. (d) This polymerization mechanism leads to the formation of double-stranded, half-staggered linear chains known as protofibrils. (e) Later on, when the FPBs are also removed, the protofibrils aggregate laterally via *bB* interactions, giving rise to fibers of increasing size.

cal length, they aggregate side-by-side and form fibers of increasing diameter [Fig. 1(e)]. Notice that the protofibrils inside each fiber may not be densely packed, but intertwined with solvent molecules, so that the fiber density may be sensibly smaller than the density of protofibrils. Depending on the physical–chemical conditions of the solution, the fibers grow following different modalities, and eventually link to each other and form a three-dimensional gel. For references and more detailed information on the fibrinogen structure and its polymerization mechanisms, see Refs. [1–3].

Fibrin gels have been the object of intense investigations since the late 1940s, mainly using electron microscopy, with light scattering techniques also playing an important role (see Refs. [2] and [3], and references therein). These studies have shown that the physical properties of the gel as well as its physiological functionality are determined, to a large extent, by the structure and morphology of the network. This depends on the size of the fibers, on the extent of their branching, on their spatial distribution, and also on the average distance between them, which corresponds to the gel mesh size. The gel structure can be controlled by changing the physical–chemical parameters of the gelling solution, such as salt concentration (e.g., ionic strength) and type, *p*H, kind of activating enzyme, and can be continuously varied between two limiting classes in which fibrin gels are customarily classified: ''coarse'' and ''fine'' gels. ''Coarse'' gels are large-pore gels made of thick fibers, while ''fine'' gels are narrow-pore gels made of thin fibers. An updated summary of some of the different possible gel structures and their dependence on the polymerization conditions can be found in Ref. [7], and references therein.

The aim of this paper is to present a light scattering study of the structure and growth kinetics of ''coarse'' fibrin gels grown under quasiphysiological conditions. The static scattered intensity distributions $R(q)$ of the aged gels were measured in absolute units by combining the low-angle elastic light scattering (LAELS) and the classical light scattering (CLS) techniques, covering an overall wave-vector range of about three decades, from $q \sim 3\times10^2$ to $q \sim 3\times10^5\ \mathrm{cm}^{-1}$. The main features of these distributions were the very low intensity scattered in the limit of zero angle, the presence of a peak at low q's, and the presence of a sharp rolloff at high q's, beyond which $R(q)$ decays very rapidly. The data were interpreted in terms of a simple structural model and a single fitting function, able to reproduce the $R(q)$ behavior over the whole wave-vector range, was devised. This allowed the estimate of the fiber diameter d, the gel crossover length ξ, the mass fractal dimension D_m, and surface fractal dimension D_s of the fibers. By measuring the intensity in absolute units, it was possible to recover also the density ρ of the fibrin fibers and have an independent measure of their size.

The kinetics of formation of the gels was studied by measuring the LAELS distributions at different times after the addition of thrombin, and the behavior of the parameters characterizing the gels structure was studied as a function of time. A simple growth mechanism was devised as the outcome of this study. Several measurements were also taken on gels grown under the same physical–chemical conditions of the gelling solution, but at different fibrinogen concentrations c_F; however, it is beyond the purpose of this work to describe how the gel parameters depend on c_F, and therefore these results will be presented elsewhere (F. Ferri *et al.*, in preparation).

This article is organized as follows: in Sec. II we describe the procedure followed for preparing and handling the sample and give a brief description of the light scattering techniques together with their relative experimental setups; the experimental data taken on both aged and growing gels are presented in Sec. III; Sec. IV is devoted to illustrate the data analysis and present a simple model capable of describing both the kinetics of the gelation process and the structure of the aged gel; the main results are then summarized in Sec. V.

II. MATERIALS AND METHODS

A. Materials

Human fibrinogen and thrombin were purchased from Calbiochem, San Diego, CA (Cat. No. 341576, lot B10707) and Sigma-Aldrich, Milano, Italy (Cat. No. T-6759, lot 104H9314, ~2000 NIH units/mg protein), respectively. Tris-hydroxymethyl-aminomethane free base (Tris) and the hydrochloride form (Tris-HCl) and all other chemicals were of reagent-grade from Merck (Bracco, Milano, Italia). Double-distilled water was always used throughout this study.

B. Sample preparation and control

Solutions of human fibrinogen were purified by using size-exclusion chromatography on a 100×1.5 cm glass column (Pharmacia Biotech Italia, Milano, Italy) filled with Sepharose CL-4B (Pharmacia Biotech Italia) eluted at 3 ml/h with 0.1 M NaCl, 1 mM EDTA-Na_2, 0.05 M Tris-HCl, *p*H 7.4 buffer to remove large aggregates. The fibrinogen ''monomer'' peak fractions were pooled, divided in aliquots, quick-frozen, and stored at -20 °C. Just prior to analysis, aliquot(s) were rapidly thawed at 37 °C. The solution was then diluted in the appropriate buffer to reach the desired final fibrinogen concentration and filtered through a 0.22 μm pore low retention filter (Millex-GS, Millipore, Milano, Italy) directly into the scattering cell, which was previously carefully washed with clean, 0.22-μm-filtered water to nearly dust-free conditions and then dried under vacuum. To start the reaction, human thrombin was added under rapid stirring to the fibrinogen solution to a final molar ratio of 1:100. Fibrin cross-linking due to the enzyme ''factor XIIIa,'' which may copurify with fibrinogen, was inhibited by the addition of EDTA-Na_2 to the buffer solutions.

Fibrinogen concentration was determined spectrophotometrically by measuring its absorbance at 280 nm (A^{280}) and assuming an extinction coefficient $\varepsilon^{280}=1.51\,\mathrm{ml\,mg^{-1}\,cm^{-1}}$ [8]. Corrections for scattering contributions were accounted for by subtracting the solution absorbance at 320 nm.

The integrity of the sample was controlled via gel electrophoresis as previously described [9]. The analyses showed that our ''purified'' samples were at the same level of heterogeneity as the ''physiological'' fibrinogen, e.g., the one circulating in blood vessels [10].

C. Elastic light scattering techniques

Elastic light scattering techniques are based on the measure of the angular distribution of the intensity of the light elastically scattered from a sample. In the theory of elastic light scattering, the light scattered out of the incident beam is due to the presence of local fluctuations of the dielectric constant of the medium ε over the entire scattering volume V. In many cases, such as for colloidal, macromolecular, or gel systems, these fluctuations are due to corresponding fluctuations of the sample density. Thus the intensity distribution $R(q)$ of the scattered light can be written, in absolute units, as [11]

$$R(q)=\frac{\pi^2}{\lambda_0^4}\left(\frac{\partial\varepsilon}{\partial\phi}\right)^2\int_V\langle\delta\phi(0)\,\delta\phi(\mathbf{r})\rangle e^{i\mathbf{q}\cdot\mathbf{r}}d\mathbf{r}, \tag{1}$$

where q is the scattering wave vector, λ_0 the vacuum wavelength of the light, ϕ the sample volume fraction, and $\partial\varepsilon/\partial\phi$ can be determined via the Lorentz-Lorenz relation [12]. The magnitude of q is related to the scattering angle θ by the relation $q=4\pi n/\lambda_0\sin(\theta/2)$, where n is the refraction index of the medium. $R(q)$ is customarily called Rayleigh-ratio and represents the power scattered by the sample per unit solid angle, per unit incident power, and per unit length of the scattering volume and is expressed in $\mathrm{cm^{-1}}$.

When the sample can be assimilated to a solution or dispersion of monodisperse interacting particles, the overall sample density–density correlation function $\langle\delta\phi(0)\,\delta\phi(\mathbf{r})\rangle$ can be expressed as the convolution of the single particle correlation function and the pair correlation function which describes the spatial correlations among particles. In this case, Eq. (1) can be written as [12]

$$R(q)=KcMP(q)S(q), \tag{2}$$

where K is the optical constant given by $K=(4\pi^2/N_A\lambda_0^4)n^2(\partial n/\partial c)^2$ with N_A being the Avogadro number, c the sample concentration (mg/ml), $\partial n/\partial c$ the refractive index increment of the solute (ml/mg), and M the particle molecular weight (g/mole). The form factor $P(q)$ and the structure factor $S(q)$ are dimensionless quantities given by

$$P(q)=\frac{\int_v h(r)e^{i\mathbf{q}\cdot\mathbf{r}}d\mathbf{r}}{\int_v h(r)d\mathbf{r}}, \tag{3a}$$

$$S(q)=1+\frac{N}{V}\int_V[g(r)-1]e^{i\mathbf{q}\cdot\mathbf{r}}d\mathbf{r}, \tag{3b}$$

where $h(r)$ is the single particle density–density correlation function, $h(r)=\langle\rho(0)\rho(r)\rangle$, with ρ and v being the particle density and volume, respectively, while $g(r)$ is the pair correlation function given by

$$g(r)=\left(\frac{V}{N}\right)^2\frac{1}{V}\sum_{i\neq j}^{N}\delta(r+\mathbf{r_i}-\mathbf{r_j}), \tag{3c}$$

with $\mathbf{r_i}$ being the particles coordinated and N/V the particle number density. $g(r)$ is such that $g(0)=0$ and $g(\infty)=1$. When the particles are not correlated $[g(r)=1]$, $S(q)=1$ for any q, and one finds the well-known result for dilute solutions [12]. Conversely, when the particles are correlated $[0<g(r)<1]$, $S(q=0)$ is always <1, and tends to 1 only asymptotically for q values much larger than the reciprocal of the length scales over which the particles are correlated.

Equation (1) shows that density fluctuations characterized by a length scale ζ give contribution to the light scattered at q values given by $q\sim2\pi/\zeta$. Therefore by measuring the intensity of the light scattered within a range $[q_{\min},q_{\max}]$, it is possible to probe length scales in the range $2\pi/q_{\max}<\zeta<2\pi/q_{\min}$.

D. Experimental setup

In order to probe a range of ζ as large as possible, we utilized two different elastic light scattering instruments operating over different q ranges. The first one is a low-angle elastic light scattering (LAELS) instrument whose standard layout is described in detail in Ref. [13]. The actual layout utilized in this work is slightly different and is sketched in Fig. 2. The sample was contained in a square quartz 2 or 5 mm thick cell placed inside a temperature controlled metal block kept at 25 ± 0.1 °C. The cell was placed along the converging beam at a distance z from the detector, which is located in correspondence to the focal plane of the lens. The

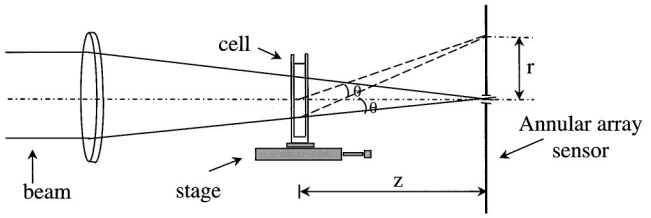

FIG. 2. Schematic diagram of the optical layout for the low-angle elastic light scattering (LAELS) instrument.

detector is made of an array of 31 annular photodiodes whose thickness and distances r from the optical axis are scaled logarithmically, so as to cover a large range of the scattering angle $\theta = tg^{-1}(r/z)$. The cell holder is clamped onto a computer-controlled translation stage that allows changing the distance z in the range 150–50 mm. In this way the θ range (in the medium) can be varied from $\sim 0.15°$–$15°$ to $\sim 0.05°$–$5.0°$, with a corresponding overall wave-vector range from $\sim 1.2\times 10^2$ to $\sim 3.3\times 10^4\,\mathrm{cm}^{-1}$. However, due to stray light problems, and to the fact that the innermost photodiodes are very thin, the instrumental sensitivity is highly dependent on q. Consequently, the actual minimum detectable angle is somewhat higher that the one reported above, and depends on the particular sample being studied. For the gels studied in this work, the practical q range was from $\sim 3\times 10^2$ to $\sim 3\times 10^4\,\mathrm{cm}^{-1}$. A tiny hole in the center of the sensor ensures that the transmitted beam passes clear off the sensor plane and allows the measurement of the sample turbidity. The instrument was calibrated by using latex spheres (from Duke Scientific Corporation., Palo Alto, Ca) of known (certified) diameters and concentrations. Since the electronics allows the sampling of the data at a rate (~ 0.1 s) which is much faster than the typical evolving times of the system, the kinetics of the gelation process can be easily studied with this instrument.

The second technique, called classical light scattering (CLS), is much more common and operates at larger angles, typically from $\sim 15°$ to $\sim 150°$. In this work the CLS instrument was an ALV/SLS-5000 system from ALV, Langen, Germany, equipped with a 4 W argon laser (Innova 70, Coherent, FRG) operating 488 nm and delivering onto the sample an average power of 100–200 mW. The beam was focused to a spot (at $1/e^2$) of $\sim 50\ \mu$m and the detection of the scattered light was carried out with a monomode fiber coupled to a photomultiplier, both mounted on a stepping motor-controlled rotating arm. The sample was contained in a cylindrical cell (8 mm inner diameter) immersed in a toluene-filled index-matching vat whose temperature was controlled to $25\pm 0.1\,°\mathrm{C}$. In this instrument, the usable wave-vector range varies from $\sim 4\times 10^4$ to $\sim 3\times 10^5\,\mathrm{cm}^{-1}$. Due to nonergodicity of the sample and to the monomode fiber detection that selects a single coherence area, the data were accumulated by averaging the scattered intensity over different spatial configurations. This was realized by simultaneously rotating and vertically translating the scattering cell during the measurements. Since the correlation time of the still sample ($\sim$10–100 ms) is much longer than the time required to change configuration, the latter one was estimated by measuring the decay time of the intensity–intensity correlation function acquired while the sample was moving. Depending on the detected wave vector, this value ranged from ~ 0.2 to ~ 2 ms. Thus in order to have approximately 10^5 independent measurements, the overall measuring time T was varied from ~ 20 to ~ 200 s. Previous utilization of this instrument for dynamic light scattering studies on fibrin gels can be found in Ref. [14].

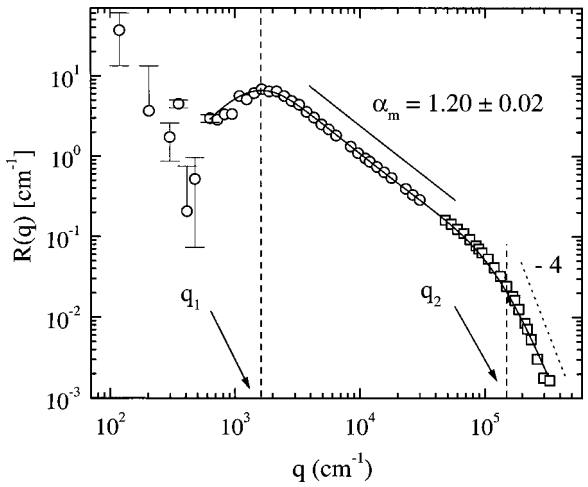

FIG. 3. Log-log plot of the scattered intensity distribution $R(q)$ as a function of the wave vector q for an aged fibrin gel prepared at the fibrinogen concentration $c_F = 0.24$ mg/ml, in a 0.1 M NaCl, 0.05 M TRIS, 1 mM EDTA, pH 7.4 buffer solution. The data have been taken by using LAELS (circles) and CLS (squares) techniques. The two dashed vertical lines and the arrows indicate the q values at which the crossovers between the three regimes described in the text take place. The average gel crossover length is $\xi \sim 4.4/q_1 \sim 27\ \mu$m, while the average fiber size is $d \sim 2.1/q_2 \sim 132$ nm (see text). The solid curve passing through the data is the result of fitting the data with Eq. (4) (see Sec. IV B). The solid straight line shows the power law decay of $R(q)$ characterized by the exponent α_m. The dotted line shows a slope of -4 indicating the expected intensity decay for a system with sharp and smooth interfaces between the scattering and hosting media.

III. EXPERIMENTAL RESULTS

In this section we will illustrate the results of our light scattering characterization of fibrin gels. The steady-structure of an aged gel will be described in Sec. III A, while the kinetics of the gelation process is reported in Sec. III B.

A. Structure of an aged gel

Figure 3 shows the intensity distribution $R(q)$ scattered from an aged fibrin gel as a function of the wave vector q. The data were taken on two different samples prepared under the same conditions by using the LAELS (circles) and CLS (squares) techniques. The samples were grown in a 0.1 M NaCl, 0.05 M Tris-HCl, 1 mM EDTA-Na_2, pH 7.4 buffer solution at $T = 25\pm 0.1\,°\mathrm{C}$, with fibrinogen concentration $c_F = 0.24$ mg/ml and molar ratio thrombin/fibrinogen $= 0.01$. The data were collected when the gels were already aged,

i.e., after a time long enough that their structures have already attained a steady-state form, with a consequent stable scattered intensity distribution. The data corresponding to CLS were rescaled by a fixed factor so as to join smoothly to the LAELS data (see Ref. [9] for details). The figure shows that there are three different regimes, delimited by the two wave vectors q_1 and q_2. For $q_1<q<q_2$, $R(q)$ decays as a power law function, $R(q)\sim q^{-\alpha_m}$, characterized by the exponent $\alpha_m\sim 1.20$. Thus in this q interval the gel exhibits a self-similar structure, and we will see in Sec. IV B that the exponent α_m represents a good estimate of its mass fractal dimension D_m. For $q>q_2$ there is a crossover to a behavior typical of surface fractals in which $R(q)$ decays much faster, consistently with a power law behavior characterized by an exponent of $\alpha_s\sim 4$, or larger. The intercept of the two power law behaviors defines the crossover wave vector q_2 and allows estimating the weight average diameter $\langle d\rangle_{\rm wt}$ of the gel fibers. This is given by $\langle d\rangle_{\rm wt}\sim 2.1/q_2$ (see Sec. IV C), and in the case of Fig. 2 is $\langle d\rangle_{\rm wt}\sim 130$ nm. Finally, for $q=q_1$, $R(q)$ exhibits a maximum beyond which it decreases toward smaller values. At these wave vectors, the scattered intensity is only slightly larger than the blank signals, as evidenced by the increasingly larger error bars. The peak indicates [15] the presence of a long-range order in the structure of the gel, which can be characterized in terms of a characteristic length scale, or crossover length ξ. This means that for length scales much smaller than ξ (but larger than d), the gel behaves as a fractal system. Conversely, for a length scale much larger than ξ, it can be considered a homogeneous system, which scatters only a little light. In Sec. IV A the gel will be modeled as a collection of fractal blobs closely packed together, and ξ will be interpreted as the average blob size. Its quantitative relation to the peak position is $\xi\sim a/q_1$, where $a\sim 4.4$ is a dimensionless parameter whose value is derived from the model. For the data of Fig. 2, $\xi\sim 27\ \mu$m. The solid line reported in the figure is the best fit of the data to the function (4) which will be discussed in Sec. IV B.

B. Kinetics of growth

To investigate the kinetics of growth, we have taken a number of LAELS measurements in the course of the gelation process. This is shown in Fig. 4, where $R(q)$ is plotted as a function of q for different times after the addition of thrombin to the fibrinogen solution ($t=0$ time). The gel had $c_F=0.81$ mg/ml and was prepared under the same conditions as that of Fig. 3. The figure shows that after approximately 150–200 s, a time that is very small compared with the overall duration of the gelation process, the intensity distribution has already attained its final shape. Later on, this shape remains substantially the same, but the intensity amplitude increases constantly until the final steady-state structure is formed, at ~2000 s. Intensity distributions taken over the next 1.5 h were identical, within experimental errors, to the one taken at ~2000 s. At a time of ~6600 s, the sample was moved closer to the detector, and its scattered intensity was measured also at larger wave vectors, up to $3.3\times 10^4\ {\rm cm}^{-1}$. The turbidity associated to the upper curve of Fig. 4 was $\tau\sim 2.5\ {\rm cm}^{-1}$, which corresponds, in a 2 mm thick cell, to an attenuation of ~40%. Thus one may expect that multiple scattering strongly affects the shape of $R(q)$, but this is not the case. Indeed, the last ~4 to 5 curves of the figure all exhibit the same shape, regardless of the fact that their amplitudes (and therefore their turbidities) are quite different, varying by a factor of ~10 or larger. The reason why, at very low angles, the multiple scattering is not very relevant is explained in Ref. [16]. The solid lines are the best fits of the data to the function (4) (see Sec. IV B), and allowed to estimate, for each $R(q)$, the peak position of the wave vector $q_{\rm peak}$.

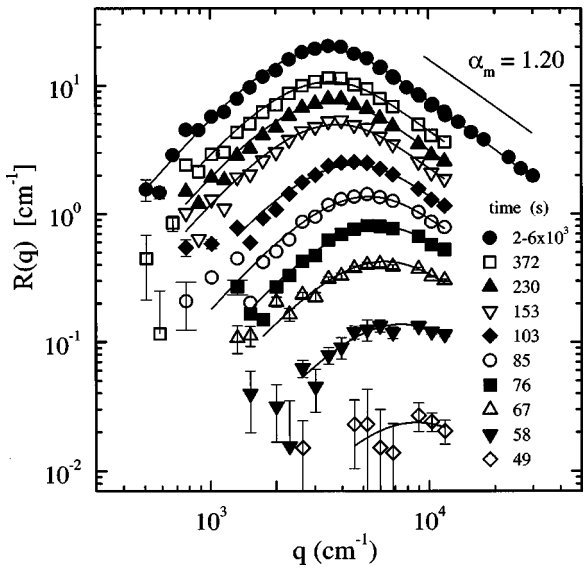

FIG. 4. LAELS study of the kinetics of gelation for a fibrinogen solution leading to a gel similar to that of Fig. 3. The fibrinogen concentration was $c_F=0.81$ mg/ml, all the other parameters being the same as those reported in Fig. 3. The different data refer to $R(q)$ measured at different times after the addition of thrombin to the fibrinogen solution ($t=0$ time). The solid lines are the best fits to Eq. (4) of the text (see Sec. IV B). The upper curve refers to data taken during a time interval between 2000 and 6000 s and corresponds to the aged gel. For the sake of clarity, only the error bars associated to some of the noisiest points have been reported. The data show that, while the amplitude of $R(q)$ increases constantly with time, its angular distribution attains a steady-state shape after approximately 150–200 s, with $q_{\rm peak}\sim 3500\ {\rm cm}^{-1}$ and $\alpha_m\sim 1.20$.

A quantitative analysis of the data of Fig. 4 was carried out by reporting in Fig. 5 the time behavior of some of the gel parameters, namely the sample turbidity τ [Fig. 5(a)], the Rayleigh ratio $R(q_a)$ at a wave vector q_a ($10^4\ {\rm cm}^{-1}$) belonging to the fractal regime [Fig. 5(b)], the peak position $q_{\rm peak}$ [Fig. 5(c)], and the decay exponent α_m [Fig. 5(d)]. The figure shows that there are three temporal regimes, given by time scales smaller, comparable, or much larger than a latency time of ~50 s that we identify as the ''networking time,'' t_n. For $t\leqslant t_n$, the turbidity and the scattered intensity are very small and only barely detectable with the instrument, until, at $t\sim t_n$, they both undergo an abrupt discontinuity and start to grow very fast. Contemporarily, a peak appears in the scattered intensity distribution and the exponent α_m starts to be detectable. It is worth noting that our

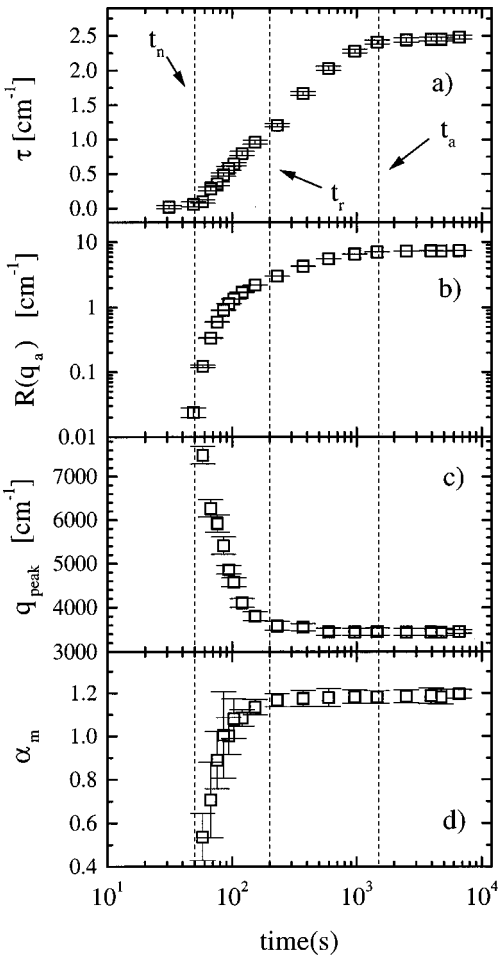

FIG. 5. Behavior of the sample turbidity (a), Rayleigh ratio at $q_a = 10^4$ cm^{-1} (b), peak position (c), and exponent α_m (d) as a function of time for the same sample as that of Fig. 4. The vertical lines at the ''networking'' time t_n, the ''ripening'' time t_r, and the ''aging'' time t_a delimit the three temporal regimes described in the text.

definition of t_n is almost equivalent to the ''clotting time'' defined in Ref. [17]. During the successive times ($t \geqslant t_n$), τ and $R(q_a)$ continue to grow fast, α_m changes from $\leqslant 1$ to ~ 1.2, and q_{peak} moves toward smaller q's, reaching a stable value a factor of ~ 2 smaller. This is the time period during which the gel structure ripens until $R(q)$ attains its final steady-state shape (see Fig. 4) at a time of ~ 200 s that that we have labeled as ''ripening time,'' t_r. Later on ($t \geqslant t_r$), only an increase of the turbidity and of the amplitude of $R(q)$ is observed, without any change of its shape, as evidenced by the fact that both q_{peak} and α_m remain constant. This increase stops at the ''aging time,'' t_a, when the gel has attained its final steady-state structure. Thus during this final phase ($t_r < t < t_a$), the gel structure remains fixed and the gel growth consists only in a thickening of its fibers, with no change in their relative positions. It is interesting to note that the time required for forming the final aged gel is much longer that the networking time ($t_a \sim 40 t_n$,) and that the overall increase of $R(q_a)$ with respect to its value at t_n is fairly large, approximately by a factor of ~ 300.

IV. DATA ANALYSIS AND DISCUSSION

In this section, we will address four issues associated with the data analysis. First of all, we will propose a simple model capable of describing the main features of the steady-state gel structure (IV A). Then, based on this model, we will describe the function used for fitting the data and discuss the physical meaning of its parameters (IV B). Third, we will address the problem of how to obtain a quantitative estimate of the fiber size from the data at very large wave vectors (IV C). Lastly, the kinetics data will be processed according to a simple growth model, and self-consistency arguments for supporting such a model will be presented (IV D).

A. Modeling of the steady-state gel structure

When a ''coarse'' fibrin gel has attained its final steady-state structure, it looks like (from electron microscopy (EM) pictures, see, for example, Ref. [18]) a random network of many thick fibers entangled together to form a very complex structure. The fibers, whose diameter can be as large as hundreds of nanometers, appear to be very inhomogeneous: some of them are long and straight, some are bent, some branch off, and their distribution in space does not appear to be uniform as well. The void spaces among the fibers are also very inhomogeneous, and in some cases, can be very large, up to several microns. Moreover, depending on the physical–chemical conditions under which the gel has been grown, the EM pictures are very different and show quite different gel structures and morphologies (see, for example, Ref. [19]). Nevertheless, in spite of this large variety of cases, and on the basis of the nice features exhibited by the scattered intensity distribution of Fig. 3, a very simple model capable of describing the gel structure can be proposed.

Let us imagine the gel as a dense collection of N blobs pervading the entire scattering volume V. Suppose that each blob is made of an assembly of n ($n \gg 1$) segments which can be sketched as cylindrical segments with an average diameter d and an average length l. The segments represent the blobs ''building blocks'' (not to be confused with the fibrinogen monomers), are bonded together end-to-end, and at each bonding site they can either be linked to only another segment giving rise to linear chains, or branch off producing a somewhat ramified structure.

In the first case the blobs are wormlike chains characterized by a contour length $L = nl$, a persistence length l_p, and an end-to-end distance h which is function of L and l_p. As is known [20], depending on the chain flexibility, l_p can vary from a minimum value of $l/2$, which corresponds to random coils, to values much larger than L for which the chain behaves as a rigid cylinder. In the second case, the blobs are branched polymers with a morphology which depends on the branching mechanism. Both types of blobs are, in principle, consistent with the observed power law decay of the scattered intensity. If the blobs are wormlike chains, this behavior may be due to a large polydispersity in the persistence length of the chains. The result is a self-similar structure characterized by the Flory exponent ν [20], according to which the end-to-end distance of the chain h scales as $h \sim l n^{\nu}$ and the scattered intensity decays as $R(q) \sim q^{-1/\nu}$ (an

example of a polydispersity in l_p resulting in such a structure is reported and discussed in the Appendix).

Alternatively, considering the blobs as branched polymers, they may be described in terms of fractal theory [21], with the mass fractal dimension D_m depending on the physics of the polymerization process. In this case the average size ξ of the blob scales as $\xi \sim l n^{1/D_m}$ and the scattered intensity decays as $R(q) \sim q^{-D_m}$. Therefore the two descriptions appear to be equivalent provided that $\nu = 1/D_m$ and that the end-to-end distance h represents a good estimate of the blob size, i.e., $h \sim \xi$. The range of length scales over which this is valid is set, at the upper limit, by the size of the blob (h or ξ) and, at the lower limit, by the segment length l.

Given this equivalence, we will adopt the description in terms of fractals. Thus, even without knowing the polymerization mechanism and/or the microscopic details of the segment–segment interactions, the gel can be assimilated to a collection of fractal blobs of a given size ξ and characterized by a mass fractal dimension D_m. In order to account for the observed peak in the scattered intensity distribution, the blobs must be arranged in space with a long-range order spatial distribution. The simplest way to do this is to suppose that the blobs are closely packed, so that their overlap concentration [20] is equal to the overall sample concentration, and their average distance $\xi_0 \sim \langle N/V \rangle^{-(1/3)}$ is equal to their average size, i.e., $\xi \sim \xi_0$. This assumption is supported by the very low intensity scattered in the limit of zero angle (see the discussion in Sec. IV B).

As a concluding remark, it may be worth noticing that the parameter l is somehow related to overall flexibility of the network because it sets the minimum persistence length of the fibers. Thus we may expect that gels with more rigid fibers would be modeled by blobs with longer segment lengths.

B. Fitting function

As described in Sec. II C, the intensity distribution scattered by a collection of interacting blobs (or particles) can be written as the product of a structure factor $S(q)$, which describes the spatial correlation between each blob's center of mass, and a form factor $P(q)$, which describes the internal structure of the blobs [see Eq. (2)]. After several trials, we found that a function which is able to reproduce the overall behavior of the data over the entire wave-vector range of Fig. 3, is the following

$$R(q) = KcM\underbrace{\left[1-\beta e^{-(\gamma \xi q)^2}\right]}_{S(q)}\underbrace{\left[\frac{1}{\left[1+(q\xi/\pi)^2\right]^{(D_m/2)}}+\left(\frac{l}{\xi}\right)^{D_m}\right]}_{A(q)}\underbrace{\frac{1}{\left(1+q^2d^2\sqrt{\frac{l}{32d}}\right)^{(\alpha_s/2)}}}_{B(q)} \tag{4}$$

where the product $A(q)B(q)$ plays the role of the ''particle'' form factor $P(q)$. Here K is the optical constant defined in Eq. (2), c is the blobs concentration, and M is the blob molecular weight which is given by the product of the segment mass $m = (\rho \pi/4) l d^2$ times the number $n \sim (\xi/l)^{D_m}$ of segments per blob, i.e.,

$$M \sim N_A \frac{\rho \pi}{4} l^{1-D_m} \xi^{D_m} d^2, \tag{5}$$

where ρ is the segment density. One may notice that Eq. (5) provides the exact expression for the blob mass when this is either a stiff cylinder ($D_m = 1$; $\xi = L$) or a random coil chain ($D_m = 2$; $\xi = \sqrt{Ll}$). Equation (4) depends on many parameters, namely, ρ, β, γ, ξ, D_m, d, l, and α_s. Of these, only ρ, ξ, D_m, and d were actually left to be floating in the fitting, the remaining ones being fixed to values determined according to physical considerations. These are going to be discussed below together with a thorough description of the three factors $S(q)$, $A(q)$, and $B(q)$. Notice also that Eq. (4) describes a ''monodisperse'' system, i.e., a system in which all the blobs have the same size ξ and are characterized by the same d and l. The effects of polydispersity on these parameters will be considered in the next section.

Let us start by noticing that the recovery of the parameter ρ is a direct consequence of measuring $R(q)$ in absolute units and, of course, of knowing both c and K ($K = 4.30\ \mathrm{cm^2/g^2}$, employing a value of $\partial n/\partial c = 0.192\ \mathrm{cm^3/g}$ at 633 nm, see Ref. [22]). Indeed, the parameter ρ appears only in the prefactor of Eq. (4), thus affecting only the amplitude of the scattered intensity, not its shape. Incidentally, it should also be recalled that the density ρ of the segment which adds up to form a fiber, must not be confused with the density of the fibrinogen/fibrin monomer molecules ($\rho_F = 1.395\ \mathrm{g/cm^3}$). The latter value could also be a reasonable estimate for the two-stranded ''protofibrils.'' Instead, the segment density may be sensibly smaller, meaning that the protofibrils are not densely packed to form the fibers, but they are intertwined with solvent molecules [23].

As expected, the behavior of $R(q)$ at low q's is determined by the structure factor $S(q)$. Indeed, for $q \ll 1/\xi$, the factors $A(q) \sim B(q) \sim 1$ and $R(q) \sim (1-\beta) + \beta\gamma^2\xi^2q^2$. The

correlation amplitude is controlled by the parameter β that can vary between 0 and 1. For $\beta=0$, there is no correlation and $S(q)=1$, independently of q, while for $\beta=1$, there is strong correlation and $S(0)=0$. Except for the early phases of the gelation process (at times $t\sim t_n$), or for aged gels at the lowest concentrations, all our data are best fitted when $\beta=1$. This can be used for estimating the relative magnitude between the blob size ξ and their average distance ξ_0. Indeed, if we consider the blobs as monodisperse spherical particles with hard-sphere (HS) interactions, a value of $S_{\mathrm{HS}}(0)\sim 0$ would be attained only for a very high volume fraction ϕ, namely when $\phi\sim 0.52$ [24]. This value corresponds to the condition of close packing, i.e., when the sphere's diameter is equal to its average distance. Thus though the blobs structure and interactions are very different from the case of hard spheres, we think that when $S(0)\sim 0$, the blobs are expected to be closely packed with $\xi\sim\xi_0$. It should be pointed out, however, that the HS structure factor appears to be highly inadequate to describe our experimental data. This is because, close to the condition of close packing, $S_{\mathrm{HS}}(q)$ exhibits several peaks and oscillations, implying that the correlations extend over a range of several interparticle distances. This is very different from our measured $S(q)$ which, on the contrary, relaxes monotonically to 1 as $q\to\infty$. The reason for this behavior can be attributed either to effects of a large polydispersity in particle sizes [which smears out the oscillations present in $S_{\mathrm{HS}}(q)$], or to the fact that the particles are clearly not spherical. Examples for these two behaviors can be found in Ref. [25]. The actual expression of $S(q)$ used in Eq. (4) was found heuristically, by using a simple function capable of reproducing the data behavior at low q's.

The range over which $S(q)$ relaxes to its asymptotic value is controlled by the parameter $\gamma\xi$ appearing in the Gaussian term of $S(q)$. The behavior of the pair correlation function $g(r)$ associated to $S(q)$ can be obtained by inverting Eq. (3b)

$$g(r)=1-\frac{\beta}{(2\sqrt{\pi})^3}\frac{1}{(N/V)\gamma^3\xi^3}e^{-(r/2\gamma\xi)^2} \tag{6}$$

from which one sees that $g(r)$ has a Gaussian shape with the particles being spatially correlated over a length scale of the order of $2\gamma\xi$. In order to satisfy the constraint that $g(0)=0$ (see Sec. II C), the factor multiplying the Gaussian term must be 1, implying that

$$2\gamma\xi=\frac{\beta^{1/3}}{\sqrt{\pi}}\xi_0, \tag{7}$$

where we have used $\xi_0\sim\langle N/V\rangle^{-(1/3)}$. Thus the correlation length $2\gamma\xi$ of the system scales as ξ_0 and, since $0<\beta<1$, it is upper limited to the value of $\xi_0/\sqrt{\pi}\sim 0.56\xi_0$. Therefore a shape for $S(q)$ as that reported in Eq. (4) implies that the correlation length of the system is of the order of half the average distance between the blobs. If we recall that for our gels $\beta=1$ and $\xi\sim\xi_0$, it turns out from Eq. (7) that $\gamma=1/2\sqrt{\pi}\sim 0.28$. This is the value to which we have fixed the parameter γ in all our fittings.

As a comment, we would like to mention that we tried to fit the data with other shapes of $S(q)$ as well. For example, we used the HS structure factor, but it did not work for the reasons mentioned above. We also tried with the $S(q)$ proposed by Dietler *et al.* [26], where the correlation $g(r)$ was characterized by an exponential rather than a Gaussian decay. The results are similar, but the quality of the fitting is somewhat poorer at low q's. Lastly, we tried to interpret the data in terms of a depletion zone surrounding each blob, as recently suggested for the formation of colloidal [27] and emulsion [28] gels, or for the growth of semiconductor [29] and hard-sphere [30] crystallites. A phenomenological model based on this effect was developed by Carpineti *et al.* [31] and successfully applied to the formation of colloidal gels [27]. However, when we use the fitting function proposed in Ref. [31], the data are very poorly fitted at the lowest q's. This is comprehensible because our gels exhibit a growth kinetics that is very different form that observed in the colloidal gels of Ref. [31]. In the latter ones, the size of the clusters vary very much in the course of gelation (roughly by a factor of $\sim$10), passing from values which are much smaller than the average clusters distance, up to values comparable with this distance, when the gel is formed. Thus at the beginning, the presence of the peak in the scattered intensity is attributed to depletion effects and not to spatial correlations among clusters. Conversely, in our gels the blobs size varies very little because, from the appearing of the peak in the scattered intensity up to the final aged gel, it increases only by a factor of $\sim$2. Therefore spatial correlations appear to be responsible for this peak already from the beginning of the kinetics, and we believe that the analysis of Ref. [31] is not appropriate for our case.

We come now to discuss the form factor $P(q)$. Since each blob is an assembly of many segments, its form factor $P(q)$ can be written as the product of two terms: the structure factor $A(q)$ describing the correlation among segments and the form factor $B(q)$ of the single segment. The left-hand side of $A(q)$ represents the ''distinct'' contribution to this structure factor and was approximated to a Fisher–Burford (FB) function [32]. The factor π was introduced because it allows the recovery, for $q\xi\gg\pi$, of the exact asymptotic absolute scattering intensity for cylinders (see Sec. IV C), and, at the same time, provides a quite good approximation of the cylinders form factor at all the other values of q (maximum deviation being of the order of 10% at $q\xi\sim\pi$). It should also be pointed out that the FB function (with the factor π) represents a good approximation of the form factor of random coils as well. For these systems, the asymptotic decay is $P(q)\sim 12/q^2\xi^2$, while our model predicts $P(q)\sim\pi^2/q^2\xi^2$ with an error of $\sim -20\%$. At all the other q values, the approximation is also satisfactory with a maximum error of $\sim$22% at $q\xi\sim\pi$. In conclusion, the Fisher–Burford function describes the fractal nature of the blobs which, from length scales comparable to the basic segment length l up to the blob size ξ, behave as fractal objects characterized by a mass fractal dimension D_m. In this region ($\xi^{-1}\ll q\ll l^{-1}$), the corresponding scattered intensity decays

as $R(q)\sim q^{-D_m}$. The right-hand side of $A(q)$ is the ''self'' part of the blob structure factor and is equal to the reciprocal of the number of segments inside the blob. This contribution represents the incoherent scattering from the segments and becomes comparable with the FB function when $ql=\pi$. It should be pointed out that this contribution may affect the observed power law decay of $R(q)$ when this is measured over q values not $\ll\pi/l$. Thus the apparent decay exponent α_m, recovered by fitting the data to a power law, represents an underestimate of the fractal dimension, i.e., $\alpha_m<D_m$. An example of this effect is going to be given later on and shown in Fig. 7.

In the region dominated by the segments ($ql\gg\pi$), the scattered intensity behaves as $R(q)\sim cM(l/\xi)^{D_m}B(q)\sim Nnm^2B(q)$, i.e., $R(q)$ is given by the sum of the intensities scattered by all segments present in solutions, whose total number is Nn. The segment form factor $B(q)$ was chosen heuristically, so as to recover the expected behavior for the scattered intensity distribution from cylindrical objects with a sharp interface between them and the solvent. In this case, $R(q)$ decays asymptotically for large q's as $\sim q^{-4}$ and its amplitude is a function only of the segment diameter d, with no dependence on D_m, ξ, and l (see Sec. IV C). This is satisfied by Eq. (4) because, as soon as $\alpha_s=4$ and ql, $qd\gg1$, we obtain $R(q)\sim cd^{-1}q^{-4}$. In particular, the numerical factor 32 appearing in $B(q)$ has been introduced to ensure that also the absolute scale of $R(q)$ is correct (see Sec. IV C). More generally, if the surface of the segments is not smooth, and/or the interface between them and the solvent is not sharp, the parameter $\alpha_s\neq4$. In the case of sharp interfaces, the surface fractal dimension D_s is related to α_s by $D_s=6-\alpha_s$ [33]. Thus for a smooth surface ($D_s=2$) we have $\alpha_s=4$, while for a totally rough surface ($D_s=3$) it turns out that $\alpha_s=3$. Alternatively, if the interface is not sharp but extends over a finite range, $\alpha_s>4$ with the actual value depending on the interface profile. Our data seems to indicate a tendency to have values of $\alpha_s>4$, but this is only a vague indication because the extension of the q range over which the surface fractal regime is observed is fairly narrow, and no reliable estimate of α_s can be given. Since we observed no significant dependence of the fitting results on the value of α_s, this value was set to $\alpha_s=4$ in all our fittings.

In order to gain further insights into the meaning of all the above parameters and illustrate how these parameters determine the behavior of the fitting function (4), we report in the next two figures a series of $R(q)$ curves obtained under different circumstances. Figure 6 reports the behavior of $R(q)$, together with the three factors $S(q)$, $A(q)$, and $B(q)$ of which $R(q)$ is the product, as a function of the reduced wave vector $q\xi$. The plot was worked out by setting $\beta=1$, $\gamma=0.28$, $D_m=1.30$, $\alpha_s=4$, and $l=d=10^{-2}\xi$. Clearly, the three factors determine the behavior of $R(q)$ at three different q regions. These three regimes are represented by the three asymptotes reported in the inset of Fig. 6. One can notice that the two intercepts of the three asymptotes allow an easy estimate of the parameters ξ and d. Namely, it is straightforward to show that the two right-hand side asymptotes cross at a value q_2 given by $q_2^{4-D_m}(d^3/l^{D_m-1})=32/\pi^{D_m}$, in which the value of $\alpha_s=4$ has been used. For the specific case of cylinders ($D_m=1$) this reduces to the expected value of $q_2d=(32/\pi)^{1/3}\sim2.2$ (see Sec. IV C). For the more general case when $D_m\neq1$, we refer the reader to Sec. IV C, but we can anticipate here that, because the value recovered in our fitting is close to unity ($D_m\sim1.3$), the result is almost independent on l and remains substantially unchanged with $q_2d\sim2.1$. The two left-hand side asymptotes cross at a value $q\xi=\pi^{D_m/2+D_m}\gamma^{-2/(2+D_m)}$ (supposing that $\beta=1$). By using the values of $\gamma=0.28$ and $D_m=1.30$, one finds that $q\xi\sim3.4$. The actual peak position $q_{\rm peak}$ falls at a value that is somewhat shifted with respect to the corresponding asymptotes intercepts, e.g., $q_{\rm peak}\xi\sim4.4$.

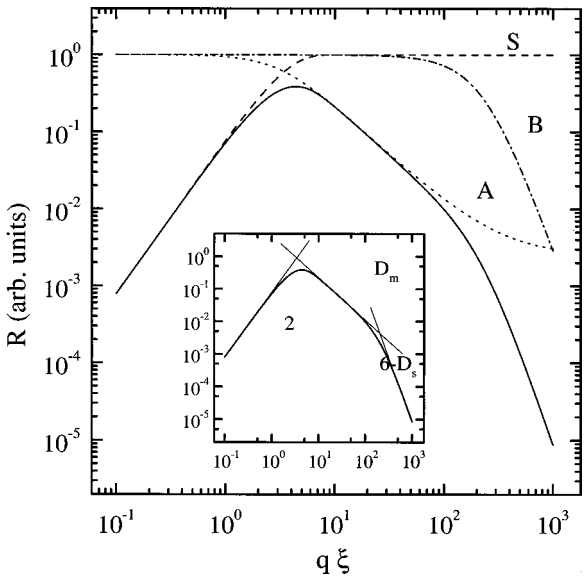

FIG. 6. Behavior of the scattered intensity distribution R (solid line) predicted by Eq. (4) as a function of the dimensionless wave vector $q\xi$. The three factors $S(q)$, $A(q)$, and $B(q)$, of which $R(q)$ is the product, are also reported as dashed, dotted, and dotted-dashed lines, respectively. In the inset, the same curve is reported together with the three asymptotes described in the text. The data have been generated with $\beta=1$, $\gamma=0.28$, $D_m=1.30$, $\alpha_s=4$, and $l=d=10^{-2}\xi$.

Figure 7 reports a series of $R(q)$ functions obtained by varying the diameter d of the fibers from 0.01 to 5 μm and supposing that the number concentration N/V of the blobs remains fixed. All the other fitting parameters were kept constant and set to the values $\beta=1$, $\gamma=0.28$, $D_m=1.30$, $\alpha_s=4$, $\xi=30\,\mu$m, and $l=0.4\,\mu$m. The figure shows that at low q's ($q\sim1/\xi$) all the curved are characterized by the same shape with their amplitude strongly dependent on d, namely $R(q)\sim d^4$, as it can be easily seen by recalling that $cM\sim(N/V)M^2$ and by using Eq. (5). Similarly, at high q's where the scattering is determined by the surface's properties, all the curves exhibit the same asymptotic power law decay and, as soon as $q\geqslant1/d$, the intensity decays as $R(q)\sim q^{-4}$. The behavior of $R(q)$ is more subtle in the central region ($1/\xi<q<1/d$) where the scattering is either dominated by the fractal blobs or by the segments, with the crossover between these two regimes occurring at $ql=\pi$ [see factor $A(q)$ in Eq. (4)]. Thus depending on the ratio l/d

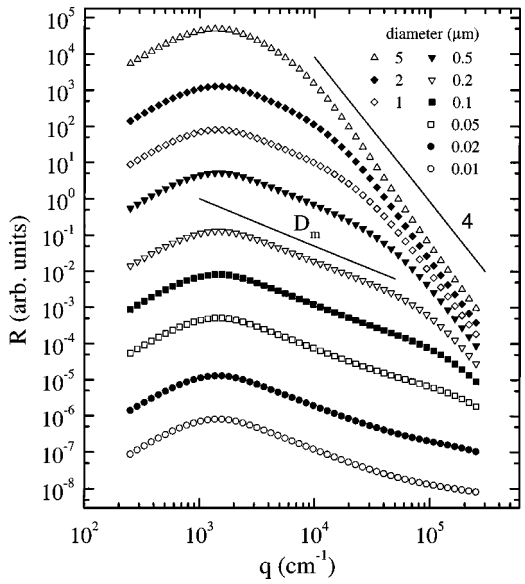

FIG. 7. Behavior of the scattered intensity distribution $R(q)$ predicted by Eq. (4) as a function of the wave vector q for gels characterized by blobs having the same number density N/V and the same structure, but different fiber diameters varying between 0.01 and 5 μm. The data have been generated by setting all the other parameters to the values $\beta=1$, $\gamma=0.28$, $D_m=1.30$, $\alpha_s=4$, $\xi=30\,\mu$m, and $l=0.4\,\mu$m.

between the segment length and its diameter, this crossover may interfere with the crossover associated to surface behavior, and $R(q)$ can exhibit very different profiles. For $l \gg d$, the crossover from the fractal region to the region where the scattering is dominated by the segments ($ql=\pi$) occurs at q values smaller than the wave vector at which the surface regime starts ($q>1/d$). Consequently, there is a wave-vector range ($\pi/l<q<1/d$) in which $R(q)$ tends to level out and exhibits an upward curvature (see bottom curve in Fig. 7). Conversely for $l \ll d$ the two crossovers swap, and by the time the segments start to dominate the scattering, they already have entered the Porod regime. Therefore the overlap between the fractal and the surface regimes leads to a broadening of the transition, with a consequent narrowing of the wave-vector range over which the fractal regime is observed and with $R(q)$ decaying faster than the expected q^{-4} behavior. The overall effect is a ''rounding'' of the curve $R(q)$ with a downward curvature (see the upper curve in Fig. 7). Lastly, when $l \sim d$, the two effects (leveling and rounding) cancel out and a nice fractal power law decay with a fairly sharp transition to the surface regime is observed. This occurs over a quite wide range of the ratio l/d, as it can be observed for the four central curves of Fig. 7 in which l/d varies between 0.4 and 4 (top to bottom). For these curves, the power law decay exponent α_m represents a good estimate of the fractal dimension D_m with deviations smaller than -10% for $1<l/d<4$ and $+10\%$ for $0.4<l/d<1$. At the same time, the crossover wave vector q_2 can be easily determined from the intercept of the two straight lines characterizing the two regimes and provides a good estimate of the fiber size, i.e., $d \sim 2.1/q_2$ (see Sec. IV C). Since our data appear to be very similar to the central curves of the figure, we expect that the segment diameter and segment length of our gel will exhibit similar magnitudes.

We conclude this section by summarizing the procedure and the results of fitting the data of Fig. 3 to Eq. (4). The fitting was carried out with the floating parameters ρ, ξ, D_m, and d, and by fixing the others to the values $\beta=1$, $\gamma=0.28$, $\alpha_s=4$, and $l=0.4\,\mu$m. While the first three values were chosen according to physical considerations as explained above, the latter one was set to an average value found by fitting the data relative to gels of different concentrations. This is probably not the best procedure because we noticed a tendency of having higher l's with higher c_F, but it helped to make the fit much more stable and reliable against the high number of floating parameters and correlations among them. On the other hand, even a marked change of the value assigned to l (for example, a factor of 2), neither produced substantial changes in the results, nor improved significantly the quality of the fitting. The outputs of the fitting were $\rho=0.42\pm0.2$ g/cm^3, $\xi=27\pm2\,\mu$m, $D_m=1.31\pm0.02$, and $d=132\pm5$ nm. Finally, it is worth noticing that a density of $\sim$0.4 g/cm^3 corresponds to fibers in which the protofibrils are highly intertwined with solvent molecules and occupies only about 1/3 of the cross sectional area of the fibers (fibrinogen density $\sim$1.395 g/cm^3). This result is consistent with that found by Carr and Hermans, who utilized a different technique based on the measure of the extinction spectrum of these gels [23].

C. Polydispersity and fiber size determination

We discuss here the effect of polydispersity on the determination of the fiber diameter d used in Eq. (4). This will be done by analyzing the behavior of $R(q)$ around the crossover region at $q \sim q_2$ and establishing a quantitative relation between the value of q_2 and the fiber diameter d. As a result of the analysis reported below, we will shown that the diameter d used in Eq. (4) is actually a weight average diameter, i.e., $d \sim \langle d \rangle_{\rm wt}$, and that it can also be estimated by using the LAELS data alone, but only if the scattered intensity is measured in absolute units.

We start our analysis by supposing that the gel can be assimilated to a solution of randomly oriented cylinders of length L and diameter d, polydisperse both in length and diameter. Since we are interested only in the large q behavior of $R(q)$, which is independent on the long range interaction between particles, we will consider the solution as being infinitely dilute and, consequently, we will put $S(q)=1$ in the expression of $R(q)$ given by Eq. (2). The presence of polydispersity transforms Eq. (3) into [12]

$$R(q)=Kc\langle M\rangle_{\rm wt}\langle P(q)\rangle_z, \tag{8}$$

where $\langle M\rangle_{\rm wt}$ is the weight-averaged molecular weight of the particles and $\langle P(q)\rangle_z$ is their z-averaged form factor. For cylinders, $P(q)$ can be calculated numerically by using the Rayleigh–Gans approximation; in particular, in the central region $L^{-1}<q<d^{-1}$, $P(q)$ can be worked out analytically ($P(q)=\pi/qL$, see Ref. [12]) and Eq. (8) becomes

$$R(q)=\pi Kc\langle M\rangle_{\mathrm{wt}}\langle L^{-1}\rangle_z q^{-1} \quad [L^{-1}<q<d^{-1}] \tag{9a}$$

$$=\frac{\pi^2}{4}KcN_A\rho\langle d^2\rangle_{\mathrm{wt}}q^{-1}, \tag{9b}$$

where ρ is the cylinders density, and we have used the relation $\langle M\rangle_{\mathrm{wt}}\langle L^{-1}\rangle_z=N_A(\pi/4)\rho\langle d^2\rangle_{\mathrm{wt}}$. Equation (9b) shows that $R(q)$ decays as q^{-1} (which is consistent with the fact that the fractal dimension of a linear object is 1) and that its amplitude does not depend on the cylinders length, but only on their squared weight-averaged diameter $\langle d^2\rangle_{\mathrm{wt}}$.

When we consider wave vectors $q>d^{-1}$, the behavior of $R(q)$ changes drastically and starts to decay much faster, asymptotically as q^{-4}. This is called the Porod regime and is a direct consequence of the presence of sharp interfaces between the scattering and hosting media. For such a system, the asymptotic behavior of $R(q)$ is proportional to the overall sample surface area per unit volume, S/V, and is given by the expression [12]

$$R(q)=2\pi KN_A\rho^2\left(\frac{S}{V}\right)q^{-4}. \tag{10}$$

If the sample is constituted by a solution of scattering particles of known morphology, then $S/V=\phi\langle s\rangle_{\mathrm{nb}}/\langle v\rangle_{\mathrm{nb}}$, where $\langle s\rangle_{\mathrm{nb}}$ and $\langle v\rangle_{\mathrm{nb}}$, are the particles number-averaged surface and volume, and ϕ is the sample volume fraction. In particular, for cylinders $S/V=4\phi\langle d^{-1}\rangle_{\mathrm{wt}}$, regardless of their length. Thus Eq. (10) becomes

$$R(q)=8\pi KcN_A\rho\langle d^{-1}\rangle_{\mathrm{wt}}q^{-4} \quad [q\gg\langle d^{-1}\rangle_{\mathrm{wt}}]. \tag{11}$$

It is worth noticing that also in this case, as for Eq. (9b), $R(q)$ does not depend on the cylinders length, but only on their weight-averaged diameter. Finally, by equating Eqs. (11) and (9b), it is straightforward to show that the crossover wave vector q_2 at which the two asymptotes cross is given by

$$q_2\langle d\rangle_{\mathrm{wt}}\sim\left(\frac{32}{\pi}\right)\sim 2.2, \tag{12}$$

where the approximation $\langle d\rangle_{\mathrm{wt}}^3\sim\langle d^2\rangle_{\mathrm{wt}}/\langle d^{-1}\rangle_{\mathrm{wt}}$ has been made. Thus we see that the crossover wave vector q_2 is related to the weight average diameter of the cylinders.

Equation (12) was worked out for the case of cylinders, i.e., particle with a fractal dimension $D_m=1$. When $D_m>1$, the analysis is very similar and is based on the expression of the blob form factor [see Eq. (4)] which, in the fractal region $(\xi^{-1}\ll q\ll l^{-1}d^{-1})$, is given by $P(q)=(\pi/q\xi)^{D_m}$. Thus by recalling that the blob molecular weight is given by Eq. (5), and by using the relation $\langle M\rangle_{\mathrm{wt}}\langle\xi^{-D_m}\rangle_z=N_A(\pi/4)\rho\langle l^{1-D_m}d^2\rangle_{\mathrm{wt}}$, it can be easily shown that Eq. (9b) is transformed into

$$R(q)=\frac{\pi^{1+D_m}}{4}KcN_A\rho\langle l^{1-D_m}d^2\rangle_{\mathrm{wt}}q^{-D_m}$$

$$[\xi^{-1}\ll q\ll l^{-1},d^{-1}]. \tag{13}$$

It is evident that now, differently from Eq. (11), the amplitude of $R(q)$ depends on the segment length l which is model dependent, and may be not known. However, since the value of D_m is not very different from unity ($D_m\sim 1.3$) and since we know that the range of variation of l cannot be very large (it is of the same magnitude of d, see Sec. IV B), the dependence of Eq. (13) on l is rather mild and leads to somewhat limited errors. For example, if the value of l is wrong by a factor of 2, the amplitude of $R(q)$ is affected only to $\sim\pm 20\%$ ($D_m=1.3$).

As far as concerns Eq. (11), this remains unchanged because in this region the scattered intensity depends only on the overall surface area of the sample. This is determined by the surface area of the segments, not by their state of arrangement or aggregation inside the blobs. In particular, if the segments are cylinders (as predicted by our model), their surface area is a function of their inverse diameter $\langle d^{-1}\rangle_{\mathrm{wt}}$ only and, therefore, Eq. (11) also depends only on $\langle d^{-1}\rangle_{\mathrm{wt}}$. Thus by equating Eqs. (13) and (11), one finds that

$$q_2\langle d\rangle_{\mathrm{wt}}=\left(\frac{32}{\pi^{D_m}}\right)^{1/(4-D_m)}\left(\frac{l}{\langle d\rangle_{\mathrm{wt}}}\right)^{(D_m-1)/(4-D_m)}\sim 2.1, \tag{14}$$

where the value 2.1 was obtained by supposing $l\sim\langle d\rangle_{\mathrm{wt}}$ and $D_m\sim 1.3$, and the same approximation as that worked out in Eq. (12) was used. Equation (14) shows that, although in principle the value on the intercept q_2 depends on D_m, l, and $\langle d\rangle_{\mathrm{wt}}$, only its dependence on $\langle d\rangle_{\mathrm{wt}}$ is relevant. Indeed, the first factor of the right-hand side of Eq. (14) is always between $\sim$2.0 and 2.2 for any D_m in the range 1–1.5, while the second factor is always $\sim 1\pm 20\%$ even for variations of the ratio $l/\langle d\rangle_{\mathrm{wt}}$ between 0.1 and 10. Thus we can conclude that Eq. (12) or (14) provides a reliable method for estimating the size of the gel fibers.

As a final comment, we would like to point out that Eq. (14) allows the estimate of the fiber's diameter without the necessity of measuring $R(q)$ in absolute units. However, we do measure $R(q)$ in absolute units. Thus in principle, we could use either Eqs. (13) and/or (11) for recovering $\langle d\rangle_{\mathrm{wt}}$. The use of Eq. (11) should be easier because the only parameters required are the (known) optical constant K and the segment density ρ which can be either estimated by fitting the overall LAELS+CLS data to the fitting function (4) or taken from literature [23]. However, as already mentioned above, the extension of the q range over which the Porod regime is observed is fairly narrow, and no reliable estimate of $\langle d^{-1}\rangle_{\mathrm{wt}}$ can be given. Conversely, the fractal regime is fairly wide, but in order to use Eq. (13), the knowledge of the segment length l is also required. As for the density, this can be estimated by fitting the LAELS+CLS data to Eq. (4) but, even when this value is not accurately known, Eq. (13) can still be fruitfully employed. This was tested by computer simulations in which synthetic data, generated according to Eq. (4), were fitted in the q range corresponding to the fractal region by means of Eq. (13). When a value of l wrong by a factor of 2 (or 0.5) was used, the average diameter recovered with Eq. (13) was correct within an accuracy of $\sim\pm 20\%$. When Eq. (13) is used for analyzing the data corresponding

to gels of Fig. 3 ($c_F = 0.24$ mg/ml) and Fig. 4 ($c_F = 0.81$ mg/ml), and the fit is carried out with $\rho = 0.42$ g/ml and $l = 0.4\,\mu$m, the average fiber diameters $\sqrt{\langle d^2 \rangle_{wt}}$ were 150 and 190 nm, respectively. The first value matches well the 132 nm obtained by fitting the overall data (LAELS+CLS) of Fig. 3 to the function (4). Thus we believe that Eq. (13) is a reliable tool for estimating the fiber diameters even when only LAELS data are available. An example of this is given in Sec. IV D, where Eq. (13) will be used for recovering the time behavior of the fiber diameter as gelation proceeds, thus providing a useful tool for checking the self-consistency of the kinetical and structural models proposed for the fibrin gels.

At this point, it may be worthwhile to compare the $\langle d \rangle_{wt}$ values obtained for the gels of Figs. 3 and 4 with EM-derived literature values. Although none were available under the very same conditions employed by us, a quite close situation was found in Ref. [18], where in one of their samples [gel of Fig. 2-A(a)], the fibrinogen concentration was $c_F = 0.5$ mg/ml, a value intermediate between the concentrations of the two gels of Fig. 3 (0.24 mg/ml) and Fig. 4 (0.81 mg/ml). All the other physical–chemical conditions were almost the same (salt type, salt concentration, thrombin/fibrinogen molar ratio, no Ca^{++} ions). From the number-average fiber diameter value reported in Table 2 of Ref. [18], we have estimated the corresponding $\langle d \rangle_{wt}$, 85 ± 20 nm. However, two corrections must be applied to this number, the first one to account for the fact that in the EM the fibers are dehydrated, the second to scale for the different concentration of the gel reported in Fig. 3. Since the ratio between the density of anhydrous fibrinogen (1.395 mg/ml) and that of the hydrated fibers measured in this work (0.42 mg/ml) is ~ 3.3, and since the density scales as the square of the diameter, the equivalent hydrated diameter is $\langle d \rangle_{wt} \sim 155 \pm 36$ nm. Finally, taking into account that the fiber diameter scales as $\sim c_F^{0.15}$ (Ferri *et al.*, in preparation), one would obtain, for $c_F = 0.24$ and 0.81 mg/ml, the values of $\langle d \rangle_{wt} \sim 140 \pm 33$ and 167 ± 39 nm, respectively, in very good agreement with our results.

D. Modeling of the growth kinetics

The data presented in Sec. III B, together with what is known from literature on the early phases of the fibrin polymerization process, can be used for describing the gel formation in terms of a very simple growth mechanism. When fibrinogen is activated by thrombin, the fibrin monomer molecules start to polymerize and give rise to linear half-staggered semiflexible chains known as protofibrils [1–3] (see Sec. I). As the polymerization proceeds, these chains grow in length and, depending on the physical–chemical condition of the gelling solution, may grow laterally as well. However, under our working conditions in which no Ca^{++} ions are present, the protofibrils are expected to grow mostly linearly with a rather broad and skewed distribution, in which long chains, intermediate oligomers, and nonactivated monomers are contemporarily present (see, for example, Ref. [22], and references therein). Now, during these early phases, the intensity scattered by the sample is very low and barely detectable only at the largest angles of the LAELS instrument. This is due to the fact that the protofibrils are very thin (~ 5 nm) and, even when they are as long as several microns, they simply do not scatter enough light. For example, the zero angle intensity scattered by a sample of monodisperse protofibrils 10 μm long and 5 nm in diameter, at a concentration of 1 mg/ml ($\sim$our highest concentration), is expected to be of the order of 5×10^{-2} cm^{-1}, a value which is well below the LAELS instrumental sensitivity at the lowest angles. However, the intensity scattered at wave vectors of $\sim 10^4$ cm^{-1} (corresponding to the largest angles) is comparable with the instrumental sensitivity, and therefore this information can be used for estimating the size of the fibers during the early times of the gelation process (see below).

When the longest chains become so long that their size ξ becomes comparable with their average distance, they start to interact and link to each other. This is the onset of gelation and occurs at a time t_n that we labeled as networking time, i.e., the time at which begins the building up of the scaffold which will be used for the growing of the final gel. The presence of the network introduces a long-range order in the system, which is responsible for the appearance of a peak in the scattered intensity distribution. Simultaneously with the network formation, there is another effect which starts to take place: while the longer chains become progressively frozen by the network, the smaller ones, whose mass fraction is still very high, can diffuse freely and keep interacting either to each other or with the frozen ones. Thus it is intuitive to understand that the fiber elongation becomes more and more inhibited with time, while their lateral growth starts to be prominent. This is a cooperative effect which gives rise to a fast increase of the scattering, as shown by the abrupt discontinuity observed in the time behavior of both the scattered intensity and sample turbidity [see Figs. 4(a) and 4(b)]. At the same time this effect is probably responsible for the observed shift of the peak position and for the increase of the asymptotic power law decay of the scattered intensity distribution. A possible explanation can be found by considering that, as the free fibers diffuse away from the pores of the network and stick to the already frozen fibers, the overall average distance between fibers increases and their structure changes as well. A second mechanism, which may contribute to the increase of the network mesh size, is the following: as the frozen fibers become thicker and thicker, they are also expected to become more rigid. Thus the persistence length of each blob (considered as a wormlike chain) should become larger, leading to an increase of the average end-to-end distance of the chain (see Fig. 10 in the Appendix). Reformulated with the language of fractal blobs, an increase of the fiber's rigidity should lead to an increase of the segment length l and, therefore, to an increase of the size ξ of a blob of a given mass [see Eq. (5)]. In both cases, the overall effect is a sort of restructuring or ripening of the gel/blobs morphology that tapers down with time, and eventually ends at a time that we indicated in Fig. 4 as the ''ripening time,'' t_r. Later on, the successive growth between t_r and t_a consists simply of a thickening of the gel fibers, consistently with the fact that both α_m and q_{peak} do not change anymore. By referring to the structural model proposed above for the aged

gel (Sec. IV B), this is equivalent to stating that during this phase all the parameters characterizing the gel structure remain fixed, with the exception of the fiber's diameter d, whose value increases with time until the aged gel is formed.

According to the kinetical picture outlined above, we can develop a simple growth model, in which the behavior of the size $d(t)$ and the concentration $c(t)$ of the frozen fibers bonded to the network can be recovered as a function of time. Let us suppose that, during the growth process, the blobs become bigger increasing their size $\xi(t)$, but maintaining their structure substantially unchanged, i.e., with the same parameters D_m, l, and ρ as those of the aged gel. Thus if the blobs are densely packed, their number density scales as $\sim\xi(t)^{-3}$, and their concentration can be expressed, making use of Eq. (5), as

$$\frac{c(t)}{c_F}\sim\left(\frac{d(t)}{d_F}\right)^2\left(\frac{\xi(t)}{\xi_F}\right)^{D_m-3}, \tag{15}$$

where the suffix F refers to the final aged gel, whose concentration is supposed to be equal to the initial monomer concentration c_F. Let us apply this model to the gel of Fig. 4, for which $c_F=0.81$ mg/ml, $d_F\sim 190$ nm, and $D_m\sim 1.20$. The latter two values were estimated by fitting the straight portion of the data corresponding to the upper curve of Fig. 4 by means of Eq. (13), in which the other parameters were set to the values $l=0.4\,\mu$m and $\rho=0.42$ g/cm^3. Likewise, the final blob size $\xi_F\sim 13$, together with the blob sizes at the earlier times $\xi(t)$, were recovered from the data of Fig. 4 according to the relation $q_{\rm peak}\xi\sim 4.4$ (see Sec. IV B). Given the crudeness of this analysis, no effect of polydispersity was considered. Note that, at the beginning of gelation, when the blobs are probably not densely packed and are characterized by values of values l, ρ, and D_m somewhat different from those of the aged gel, relation (15) may be grossly inaccurate. However, it becomes more and more reliable as the time approaches the ripening time t_r and the gels attain a steady-state structure with $\xi(t)=\xi_F$. Now, as soon as the diameter $d(t)$ of the frozen fibers becomes much bigger than the diameter of the protofibrils ($\sim$5 nm), the scattering becomes dominated by the frozen fibers, and the contribution deriving from the protofibrils can be neglected, even when the protofibrils concentration is much higher than the concentration of the frozen fibers. This is a direct consequence of the fact that, in the fractal regime, the scattered intensity scales as $R\sim cd^2$, see Eq. (13). For example, if the frozen fibers have a diameter 10 times the diameters of the protofibrils, even if their concentration is 10 times lower, they scatter 10 times stronger. Thus by neglecting the contribution of the protofibrils, we can fit the straight portions of the curves of Fig. 4 by using Eq. (13), in which the expression for $c(t)$ given by Eq. (15) is used. Consistently with the model, the fitting was carried out by fixing all the other parameters to the same values as those of the final aged gel reported above. The result, i.e., the temporal behavior of $d(t)$, is shown in the main frame of Fig. 8, in which the arrows at $\sim$50, $\sim$200, and $\sim$1500 s indicate the networking, the ripening, and the aging times, respectively. In the inset, the ratio between the concentration of the frozen fibers in the growing gel to their concentration in the final gel estimated via Eq. (15), is reported. Rather surprisingly, the concentration necessary to form the scaffold of the incipient gel at t_n is only a relatively small fraction ($\sim$10%–20%) of the overall monomers concentration c_F, the remaining $\sim$80%–90% being used for making the fibers thicker by a factor of $\sim$7. This is consistent with what was observed, a long time ago, on gels grown from a purified fibrinogen/thrombin system by Hantgan and Hermans [34], and more recently, on gels formed in recalcified plasma by Blombäck *et al.* [35]. The interesting implications of this behavior will be pointed out and discussed in the final section.

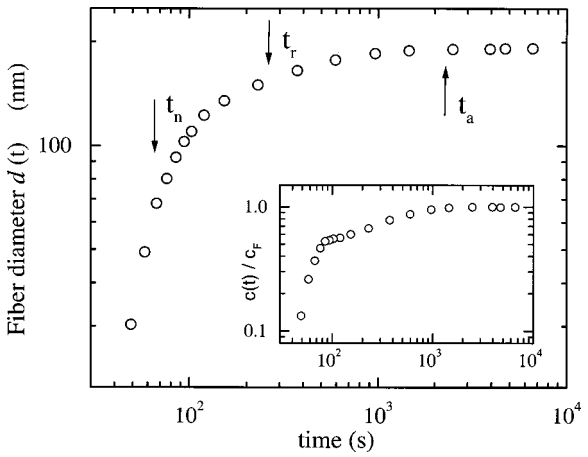

FIG. 8. Increase of the diameter of the fibers bonded to the network during gelation. The data refer to the same gel as the one described in Fig. 4. In the inset, the increase of the ratio between the concentration of the frozen fibers in the growing gel with respect to their concentration in the final aged gel, is reported. The arrows at time $t_n\sim 50$, $t_r\sim 200$, and $t_a\sim 1500$ s indicate the networking, ripening, and aging times, respectively.

We end this section with a simple analysis that can be done in order to corroborate the kinetic model proposed above. If we take the results of Figs. 5(a) and 5(b) and plot τ against $R(q_a)$ (see Fig. 9), we find out that the data (open squares) are very well-described by a power law behavior (solid line) characterized by an exponent $\beta=0.78\pm 0.02$. This means that the turbidity increases at a rate which is not as fast as the growing rate of the scattered intensity. Now, when during the course of a growing process the intensity distribution remains fixed over all the scattering angles but only an increase of its amplitude takes place, (as shown in Fig. 4), the turbidity is expected to scale linearly with the scattered intensity. This would be the case of our gels if the behavior of Fig. 4 could also be extrapolated for high wave vectors up to $\theta=180°$. However, when the gel fibers are so thick that the crossover wave vector q_2 enters the range of q's accessible to light scattering, this shape invariance holds only over the fractal regime ($q<q_2$), and the turbidity is expected to grow slower than the scattered intensity. In order to find a relation between τ and $R(q_a)$, we can apply the definition of turbidity [12]

$$\tau=\int_{4\pi}R(q)\sin^2(\phi)\,d\Omega=8\pi\int_0^1 R(x)x[1-2x^2+2x^4]dx, \tag{16}$$

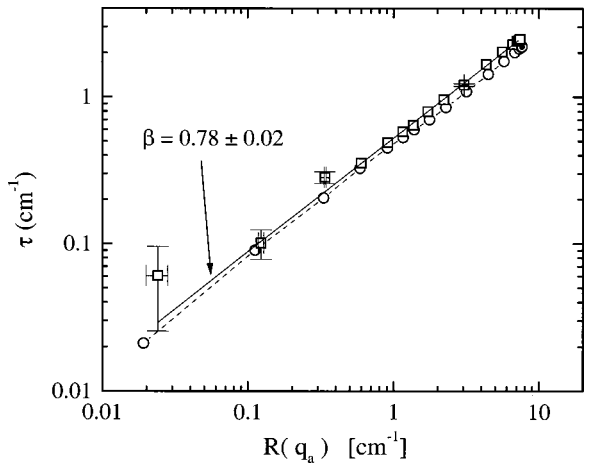

FIG. 9. Behavior of the sample turbidity τ as a function of the intensity $R(q_a)$ scattered at $q_a=10^4$ cm^{-1}, describing the same data of panels (a) and (b) of Fig. 5. The scaling between τ and $R(q_a)$ is characterized by the exponent β whose value is consistent with the growth model proposed in the text. The circles joined by the dashed line correspond to the expected behavior predicted by our kinetical model and calculated on the basis of Eq. (4). The dotted circle at the end of the dashed line represents the aged gel, see the text.

where $\sin^2(\phi)$ is the dipole term (ϕ being the angle between the laser polarization and the scattering wave vector $\mathbf{k}$) and $x=q/q_{\max}$, with $q_{\max}=4\pi/\lambda$ being the value of q in correspondence of $\theta=180°$. A rough estimate of Eq. (16) can be carried out by considering that the main contribution to the integral comes from the fractal region ($x_1=q_1/q_{\max}<x<x_2=q_2/q_{\max}$) in which $R(x)\sim d^4x^{-D_m}$ (see Sec. IV C). Indeed, for $x>x_2$, $R(x)$ decays very fast as $\sim x^{-4}$, and for $x<x_1$ the contribution to the integral is quite negligible, the value of x_1 being very small ($x_1\sim 0.01$). Thus by integrating Eq. (16) between 0 and x_2, dropping the terms in x^2 and x^4, and recalling that $x_2\sim 1/d$ [see Eq. (14)] it can be easily worked out that $\tau\sim d^{2+D_m}$. The turbidity therefore scales with the scattering intensity as

$$\tau\sim R(q_a)^{(2+D_m)/4}. \tag{17}$$

By using the value $D_m=1.2$, the exponent $\beta=(2+D_m)/4$ becomes $\beta=0.80$, which matches rather well the value of 0.78 found experimentally. It should be pointed out once again that Eq. (17) has been obtained by grossly approximating the integral (16). Nevertheless, the scaling predicted by Eq. (17) appears to be consistent with the experimental data and provides a good physical insight into the mechanism of the growing process.

As a final consistency check between the experimental data and the model proposed for the gel formation, we have calculated the expected behavior of the curve τ versus $R(q_a)$ on the basis of Eqs. (4) and (15). This was done by first obtaining τ [numerical integration of Eq. (4)] and $R(q_a)$ for the aged gel according to the parameters $\beta=1$, $\gamma=0.28$, $D_m=1.20$, $\alpha_s=4$, $\xi=12.7\,\mu$m, $l=0.4\,\mu$m, and $d=190$ nm, which were obtained from the highest curve of Fig. 4 following the same procedure used in Eq. (15). This is represented by the dotted circle shown in the upper right part of Fig. 9. Then, by using the values of $d(t)$ and $c(t)$ of Fig. 8, one can generate the entire curve τ versus $R(q_a)$ predicted by the model. The result, shown in Fig. 9 as open circles joined by a dashed line, agrees extremely well with the experimental data. It should be emphasized that this matching occurs on an absolute scale for both τ and $R(q_a)$, and that the simulation was carried out without any effective free parameter. Thus we believe that this provides rather strong evidence for the goodness of our model.

V. SUMMARY AND CONCLUSIONS

In this work we have studied the structure of fibrin gels together with the kinetics of their formation by using elastic light scattering techniques. The gels were formed by the polymerization of fibrinogen monomers under quasiphysiological conditions, and the reaction was initiated by monomers activation via the enzyme thrombin. The intensity distributions scattered from the gels were measured in absolute units over a very wide range of scattering wave vectors (up to about three decades), and were taken both while the solution was gelling and after the formation of a gel with a steady-state structure.

The data on the structure of the aged gel were interpreted in terms of a simple model, according to which a fitting function, able to reproduce accurately the data over the entire wave-vector range, was devised. Following this model, the fibrin gel can be represented as a dense collection of fractal blobs of size ξ, closely packed together so as to fill the entire sample volume. We called ξ the crossover length of the gel. The blobs are arranged in space so that their average distance is of the same order of their size ξ. This introduces a long-range order in the system, which is ultimately responsible for the observed peak in the scattered intensity distributions. Each blob is characterized by an almost linear structure, as evidenced by its fractal mass dimension close to unity, e.g., $D_m\sim 1.3$. The blobs are made by the assembly of many segments (or ''building blocks'') of length l and diameter d, which are bonded end-to-end and form semiflexible long fibers with only a few branching points. The fibers are characterized by a surface fractal dimension $D_s\sim 2$, typical of sharp interfaces between the fibers and the hosting medium, and appear to have a density ρ smaller than the density of the fibrinogen monomers. This means that, in agreement with previous reports [23], inside each fiber the protofibrils are not densely packed but intertwined with water molecules, leading to a fiber density of about 1/3 of that of the monomers.

We have also shown that, alternative to the description in terms of fractal theory, the blobs can be seen as linear semiflexible chains obtained by joining together end-to-end the segments with no branching points. However, in order to account for the observed power law decay of the scattered intensity distributions, the chains must be characterized by a large polydispersity in their persistence lengths, whose minimum value is given by $l/2$. Thus the microscopic parameter l of the model is expected to be related to the overall network flexibility.

The kinetics of the gel formation was also modeled in

terms of a very simple growth mechanism. The fibrinogen monomers polymerize into double-stranded linear chains (protofibrils) [1–3] until these are so long that they interact and link to each other. At this time, which we labeled as the networking time t_n, the onset of gelation takes place, and the scaffold for the building up of the final gel is outlined. The formation of this network is accompanied by an abrupt, rapid increase of the scattering due to the fact that the chains start to grow laterally and becomes thicker. The time t_n is much smaller than the aging time t_a required to form the aged gel. The kinetics between t_n and t_a is characterized by two different phases, which occur before and after a time that we called the ripening time t_r. For times $t_n<t<t_r$, there is a ''ripening phase,'' in which the gel structure undergoes a sort of restructuring, which leads to a slight increase of its crossover length ξ and of its fractal dimension D_m. Later on, for times $t_r<t<t_a$, a ''thickening phase'' takes over, in which the gel structure remains fixed and the growth consists only in a thickening of the gel fibers.

We tested the validity of the structural and kinetical models reported above on gels grown under the same physical–chemical conditions, but at two different fibrinogen concentrations, namely $c_F=0.24$ mg/ml (Fig. 3) and $c_F=0.81$ mg/ml (Fig. 4). These gels exhibited quite similar structures characterized by a long-range order, with similar values of D_m, but somewhat different d and a greater variation in ξ. Their kinetics were also very similar with the presence of the three temporal regimes associated to the times t_n, t_r, and t_a. This similarity is surprising, but not completely unexpected: indeed, as we pointed out at the end of Sec. IV D, the scaffold of the gel that is already present at the time t_n is built by using only a small fraction (~10%–20%) of the total initial fibrinogen mass available. The remaining ~80%–90% is still available in solution, and is mainly used for making the fibers thicker. Thus one is tempted to conclude that the fibrinogen concentration plays a minor role in determining the modalities of the gelation process, which, conversely, appear to be mainly governed by the physical–chemical conditions of the gelling solution.

At this point, it is interesting to address the issue of what is the relation between the crossover length (or average blob size) ξ and the effective gel mesh size, i.e., the average distance between the fibers in the gel. Since the observed value of the gel fractal dimension D_m is close to unity ($D_m \sim 1.3$), the blob structure is rather linear, meaning that each blob can be thought as assembly of a few semirigid chains (or fibers) grown by joining together many segments with only a few branching points. As a consequence, we expect that the average distance between fibers is not very much smaller than the size of the blob itself. Thus since the blobs are in contact to each other, we can conclude that the blob size ξ provides at least an upper bound of the overall average distance between the fibers in the gel. A quantitative relation between ξ and the effective gel mesh size would require the knowledge of microscopic details of the blob structure, which are obviously not extractable from static light scattering data only. With respect to this point, it is helpful to analyze some of the pictures of fibrin gels available in literature. By looking at the high resolution electron microscopy (EM) images of dried gels, such as those reported in Fig. 2 of Ref. [18], the gel fibers appear to be fairly entangled and curved, with a mesh size of about an order of magnitude smaller than the crossover length measured by us under similar conditions. Conversely, native fibrin gels observed by confocal laser three-dimensional (3D) microscopy [17] show a meshwork constituted by relatively straight rodlike segments which are linked mainly at denser nodes (the optical setup was able to visualize fibers as thin as ~100 nm). For instance, from the images in Fig. 3, panel D of Ref. [17], in which a gel grown under conditions similar to ours is shown, one can see that the largest pores visible are of the order of 10–20 μm, e.g., of the same order of magnitude of the crossover length ξ measured by us. It is therefore likely that the parameter represents the mesh size of the initial scaffold formed at t_n, composed by the longest fibers joined at the denser nodes. The subsequent growth leads to a thickening of these fibers and a partial filling of the voids between them, with the creation of a somewhat finer and more entangled meshwork composed by thinner, more flexible fibers. These thinner fibers appear not to have enough scattering power to affect the peak position, which therefore seems to be related to the long-range order imposed by the initial scaffold. However, the thinner fibers will contribute to the effective pore size of the gel, which from the permeation data of Ref. [17], lie somewhere in between the EM- and confocal-estimated mesh sizes. It should also be pointed out that the 3D microscopy images are taken on native (hydrated) gels, while the EM pictures are taken on dried gels. The removal of water, which occupies up to 99.9% (or even more) of the overall sample volume, requires handling procedures that inevitably compact and/or distort the gel structure. Therefore it is likely that largely spaced rodlike elements present in the native gel structure would become more bent, entangled, and coalesced fibers. Another point should also be emphasized when comparing visual images of fibrin gels with light scattering data. The first ones lead to an estimate of the gel parameters (such as d or ξ) based on number-averages. Conversely, light scattering is very sensitive to the mass of the scatterers and provides averages strongly biased by the heaviest (or largest) particles. Although we have not addressed the issue of what kind of average the estimate of ξ refers to, this is expected to be fairly larger than a number-averaged crossover length. Thus a straight comparison between the results obtained with the two techniques has to be taken with care. To verify the correctness of these ideas, and determine quantitatively how the gel parameters depend on c_F, more gels are currently being studied in our laboratories.

Finally, it is worth mentioning that a growth kinetics very similar to that reported for our gels was recently observed on two other, different types of gels, namely highly cross-linked poly(acrylamide) gels [36] and agarose-water gels [37]. In both cases, the scattered intensity distribution exhibited a peak at low angle and its amplitude increased with time without changing its position. A fractal behavior with a fractal dimension close to our values was also observed [37]. The explanation for this behavior was, however, very different from ours. In both cases the data were interpreted by supposing that, at the beginning, the scattered light is due to

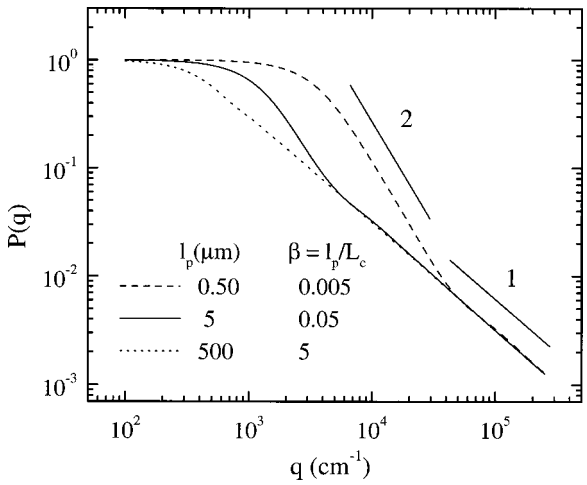

FIG. 10. Behavior of the form factor $P(q)$ for wormlike chains characterized by the same contour length $L_c=100\,\mu$m and three different persistence lengths l_p, 500 (dotted line), 5 (solid line), and 0.5 (dashed line) μm. The two segments indicate the slopes of 1 and 2, respectively, expected for rigid rods and random coils.

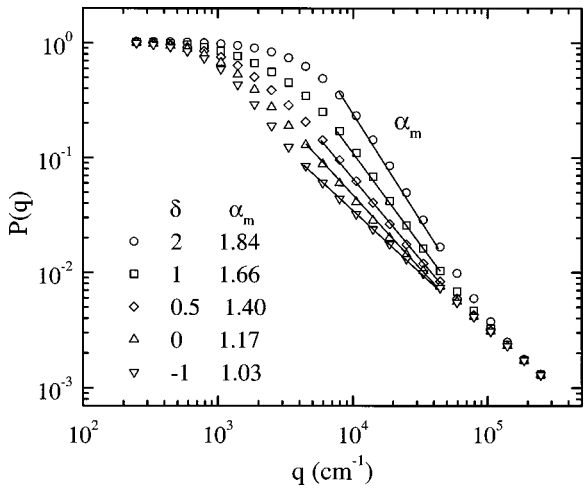

FIG. 11. Behavior of the form factor $P(q)$ for wormlike chains having the same contour length $L_c=100\,\mu$m, but polydisperse in l_p according to Eq. (A3). The polydispersity exponent δ is related to the apparent decay exponent α_m as shown in the figure.

thermodynamically driven density fluctuations associated to a phase separation process. Successively, when the onset of gelation takes over, the coarsening of the fluctuations is arrested, and only an increase in the scattered intensity is observed. Clearly, this explanation does not apply to our gels, in which no phase transition process is involved.

ACKNOWLEDGMENTS

We thank G. Dietler, M. Giglio, A. Párola, and K. Kroy for helpful discussions and suggestions. This work was supported by grants from Consiglio Nazionale delle Ricerche (CNR) to G.A. and F.F., Istituto Nazionale Fisica della Materia (INFM) to M.G., and by Agenzia Spaziale Italiana (ASI) to M.R. and F.F.

APPENDIX

In this Appendix, we want to show how a collection of wormlike linear chains polydisperse in their persistence length can give rise to a power law decay of their scattered intensity distribution. Effects of polydispersity in the contour length will be shown not to affect this feature.

Let us start by recalling how the form factor $P(q)$ for a monodisperse wormlike chain of persistence length l_p and contour length L_c looks like. The behavior of $P(q)$, whose analytical expression can be found in Ref. [38], is reported Fig. 10 as a function of q for three different chains characterized by the same $L_c=50\,\mu$m and three different l_p, 500, 5, and 0.5 μm. Depending on the ratio $\beta=l_p/L_c$ and on the q of observation, the curves exhibit quite different behaviors. For $\beta\gg1$, the chain behaves as a rigid rod and, correspondingly, $P(q)$ decays asymptotically as q^{-1} as soon as $qL\gg1$ (dotted curve). For $\beta\ll1$, the chain can be assimilated to a random coil characterized by segments of length $l_k=2l_p$ (l_k is traditionally called the Kuhn length). In this case, the asymptotic behavior of $P(q)$ depends on the value of l_p^{-1} compared with the wave vector of observation. It can be easily shown that [38]

$$P(q)=\frac{6}{L_c l_p}q^{-2},\quad R_g^{-1}\leqslant q\leqslant l_p^{-1} \tag{A1a}$$

$$P(q)=\frac{\pi}{L_c}q^{-1},\quad q\leqslant l_p^{-1}, \tag{A1b}$$

where $R_g=\sqrt{L_c l_p/3}$ is the radius of gyration of the chain. Equations (A1a) and (A1b) predict that for intermediate wave vectors [case (A1a)] the scattered intensity distribution decays as q^{-2}, as expected for random coils, while for larger q's [case (A1b)] it decays as q^{-1}, as expected for rigid rods. The wave vector q^* at which the crossover between the two regimes takes place is obtained by equating Eqs. (A1a) and (A1b) and is given by

$$q^* l_p=\frac{6}{\pi}\sim1.91. \tag{A2}$$

Thus if $q_{\max}$ denotes the maximum wave vector of the measurement and $q^*>q^{\max}$, only the random coil behavior is observed (dashed curve, Fig. 10, up to $q\sim5\times10^4\,\mathrm{cm}^{-1}$), while when $q^*<q^{\max}$, the two regions are both observed (solid curve, Fig. 10). It should be noticed that, in spite of the fact that $P(q)$ is inversely proportional to the contour length L_c, the actual scattered intensity $R(q)=KcMP(q)$ is L_c independent because $M\sim L_c$. Therefore effects of polydispersity on L_c do not change the behavior predicted by Eqs. (A1), consistent with the results obtained in Sec. IV C, Eqs. (9) and (13). Different is the case of polydispersity on the persistence length l_p which, obviously, leads to a broadening of the transition between the random coil and the rodlike

behaviors. In particular, if the distribution of the l_p's is highly polydisperse as, for example, that described by the power law decay

$$n(l_p) \sim l_p^{-\delta}, \quad l_{p_1} \leqslant l_p \leqslant l_{p_2} \tag{A3}$$

the broadening region extends over a wave-vector range $2/l_{p_2} \leqslant q \leqslant 1/l_{p_1}$. Within this range or part of this range, $R(q)$ behaves closely to a power law decay $R(q) \sim q^{-\alpha_m}$ with the exponent α_m comprising between 1 and 2 and depending on δ as shown in Fig. 11.

[1] R. F. Doolittle, Annu. Rev. Biochem. **53**, 195 (1984).
[2] Ann. N.Y. Acad. Sci. **406** (1983).
[3] B. Blombäck, Thromb. Res. **83**, 1 (1996).
[4] C. E. Hall and H. S. Slayter, J. Biophys. Biochem. Cytol. **5**, 11 (1959).
[5] J. H. Brown, N. Volkmann, G. Jun, A. H. Henshen-Edman, and C. Cohen, Proc. Natl. Acad. Sci. U.S.A. **97**, 85 (2000).
[6] Z. Yang, I. Mochalkin, L. Veerapandian, M. Riley, and R. F. Doolittle, Proc. Natl. Acad. Sci. U.S.A. **97**, 3907 (2000).
[7] E. Di Stasio, C. Nagaswami, J. W. Weisel, and E. Di Cera, Biophys. J. **75**, 1973 (1998).
[8] E. Mihaly, Biochemistry **7**, 208 (1968).
[9] M. De Spirito, G. Arcòvito, F. Andreasi-Bassi, M. Rocco, E. Paganini, M. Greco, and F. Ferri, Nuovo Cimento **20D**, 2409 (1998).
[10] Y. S. Liu, D. J. Anderson, and J. R. Shainoff, J. Chromatogr. **753**, 63 (1996).
[11] B. J. Berne and R. Pecora, *Dynamic Light Scattering* (Wiley, New York, 1976).
[12] M. Kerker, *The Scattering of Light and Other Electromagnetic Radiation* (Academic, New York, 1969).
[13] A. Bassini, S. Musazzi, E. Paganini, U. Perini, and F. Ferri, Rev. Sci. Instrum. **69**, 2484 (1998).
[14] G. Arcòvito, F. Andreasi-Bassi, M. De Spirito, E. Di Stasio, and M. Sabetta, Biophys. Chem. **67**, 287 (1997).
[15] See, for example, A. E. Gonzalez and G. Ramirez-Santiago, Phys. Rev. Lett. **74**, 1238 (1995).
[16] L. Cipelletti, Ph.D. thesis, University of Milan, Milan, Italy, 1997.
[17] B. Blombäck, K. Carlsson, B. Hessel, A. Liljeborg, R. Procyk, and N. Åslund, Biochim. Biophys. Acta **997**, 96 (1989).
[18] E. A. Ryan, L. F. Mockros, J. W. Weisel, and L. Lorand, Biophys. J. **77**, 2813 (1999).
[19] J. W. Weisel and C. Nagaswami, Biophys. J. **63**, 111 (1992).
[20] See, for example, P. G. De Gennes, *Scaling Concepts in Polymer Science* (Cornell University Press, London, 1979); M. Doi, *Introduction to Polymer Physics* (Clarendon, Oxford, 1996).
[21] See, for example, J. Teixeira, in *On Growth and Form: Fractal and Non Fractal Patterns in Physics*, edited by H. E. Stanley and N. Ostrowsky (Nijhoff, Boston, 1986).
[22] S. Bernocco, F. Ferri, A. Profumo, C. Cuniberti, and M. Rocco, Biophys. J. **79**, 561 (2000).
[23] M. E. Carr, Jr. and J. Hermans, Macromolecules **11**, 46 (1978).
[24] See, for example, J. P. Hansen and I. R. McDonald, *Theory of Simple Fluids* (Academic, London, 1986).
[25] B. Weyerich, J. Brunner-Popela, and O. Glatter, J. Appl. Crystallogr. **32**, 197 (1999).
[26] G. Dietler, C. Aubert, D. S. Cannell, and P. Wiltzius, Phys. Rev. Lett. **57**, 3117 (1986); **59**, 246 (1987).
[27] M. Carpineti and M. Giglio, Phys. Rev. Lett. **68**, 3327 (1992).
[28] J. Bibette, T. G. Mason, Hu Gang, and D. A. Weitz, Phys. Rev. Lett. **69**, 981 (1992).
[29] V. Degiorgio, G. B. Banfi, G. Righini, and A. R. Rennie, Appl. Phys. Lett. **57**, 2879 (1990); G. B. Banfi, V. Degiorgio, A. R. Rennie, and J. G. Barker, Phys. Rev. Lett. **69**, 3401 (1992).
[30] K. Schatzel and B. J. Ackerson, Phys. Rev. Lett. **68**, 337 (1992).
[31] M. Carpineti, M. Giglio, and V. Degiorgio, Phys. Rev. E **51**, 590 (1995).
[32] M. E. Fisher and R. J. Burford, Phys. Rev. **156**, 583 (1967).
[33] H. D. Bale and P. W. Schmidt, Phys. Rev. Lett. **53**, 596 (1984).
[34] R. R. Hantgan and J. Hermans, J. Biol. Chem. **254**, 11 272 (1979).
[35] B. Blombäck, K. Carlsson, K. Fatah, B. Hessel, and R. Procyk, Thromb. Res. **75**, 521 (1994).
[36] D. Asnaghi, M. Giglio, A. Bossi, and P. G. Righetti, Macromolecules **30**, 6194 (1997); D. Asnaghi and M. Giglio, Nuovo Cimento **20D**, 2175 (1998).
[37] M. Manno and M. U. Palma, Phys. Rev. Lett. **79**, 4286 (1997); M. Manno, A. Emanuele, V. Martorana, D. Bulone, P. L. San Biagio, M. B. Palma-Vittorelli, and M. U. Palma, Phys. Rev. E **59**, 2222 (1999).
[38] R. Koyama, J. Phys. Soc. Jpn. **34**, 1029 (1973).